Retrievals of mixed-phase cloud properties during the National Polar-Orbiting Operational Environmental Satellite System

Steve S. C. Ou,[1,*] K. N. Liou,[1] X. J. Wang,[1] D. Hagan,[2] A. Dybdahl,[2] M. Mussetto,[2] L. D. Carey,[3] J. Niu,[3] J. A. Kankiewicz,[4] S. Kidder,[4] and T. H. Vonder Haar[4]

[1]Department of Atmospheric Sciences, University of California, Los Angeles, California, USA

[2]Northrop Grumman Space Technology, Redondo Beach, California, USA

[3]Department of Atmospheric Sciences, Texas A&M University, College Station, Texas, USA

[4]Cooperative Institute for Research in the Atmosphere, Colorado State University, Fort Collins, Colorado, USA

*Corresponding author: ssou@atmos.ucla.edu

Received 27 October 2008; accepted 27 January 2009;
posted 10 February 2009 (Doc. ID 103157); published 3 March 2009

We describe a novel approach developed for the National Polar-Orbiting Operational Environmental Satellite System/Visible Infrared Imaging Radiometer Suite (VIIRS) to retrieve pixel-level mixed-phase cloud optical thicknesses and effective particle sizes using 0.67, 1.6, 2.25, and 3.7 μm bands reflectance/radiance. This approach utilizes lookup tables of reflectances constructed from radiative transfer simulations and a numerical iterative search method. The capability of this new approach was demonstrated using Moderate Resolution Imaging Spectroradiometer (MODIS) data as proxy to VIIRS. Two proxy scenes, 14 October 2001 over North Platte, Nebraska, during the ninth Cloud Layer Experiment (CLEX-9) and 9 November 2006 over the Great Lakes and Eastern Canada during the Canadian CloudSat/Cloud-Aerosol Lidar and Infrared Pathfinder Satellite Observations Validation Project (C3VP), were analyzed. The performance of the mixed-phase retrieval algorithm was assessed by comparison with the MODIS retrieval products, airborne *in situ* observations during CLEX-9 and CloudSat data during C3VP.

OCIS codes: 010.1615, 280.1310.

1. Introduction

Many middle-level clouds, particularly the altocumulus, altostratus, and some well-developed cirrus, contain ice particles coexisting with supercooled water droplets, down to −40 °C, and represent a large fraction of global cloud coverage (20–30%). The presence of mixed-phase clouds could play a vital role in the global radiation budget and climate system studies [1]. An ability to detect mixed-phase cloudy conditions and to retrieve their optical properties by ground-based and space-borne sensors is important for improved parameterizations of cloud microphysics, dynamics, and radiative transfer processes in numerical weather prediction and climate models [2]. This ability also enables improved predictions of in-cloud icing conditions that are critical to civil and military aircraft operations [3]. Limited lidar and laboratory observations were carried out when this importance of mixed-phase clouds was first recognized [4,5]. Parameterizations of their optical properties and model simulations of their effects on radiation budget were carried out in the past [1,6–8]. However, only recently have the aircraft *in situ* and ground-based observations of mixed-phase clouds been conducted [9–13].

0003-6935/09/081452-11$15.00/0

The mixed-phase clouds are typically mistyped in satellite cloud masking programs as either water or ice clouds. In the current National Polar-Orbiting Operational Environmental Satellite System (NPOESS)/Visible Infrared Imaging Radiometer Suite (VIIRS) cloud algorithm chain (Fig. 1 in [14]), cloud phase is determined by the NPOESS/VIIRS cloud mask, which was specifically designed to differentiate between a mixed-phase cloud and a condition of thin ice cloud overlapping water cloud. The NPOESS/VIIRS near-IR band reflectances and 8.5 and 11 μm brightness temperatures can be used to detect mixed-phase clouds, but the accuracy of the detection has not been demonstrated. In addition, there are currently no formulas for retrievals of mixed-phase cloud properties for remote sensing applications. Observational studies by Korolev *et al.* [15] suggest that relationships of parameters within mixed-phase clouds are complicated and generally poorly correlated. However, based on a series of aircraft observations, Niu *et al.* [16] found enough consistency in cloud characteristics to construct a "typical" mixed-phase cloud profile composed of three habit fractions. In the current NPOESS/VIIRS cloud retrieval program, separate cloud optical property algorithms are applied to these dual-phase pixels, which are treated either as water cloud or as ice cloud. With the availability of multiple visible and near-IR band radiance data from VIIRS, it appears that a retrieval scheme for inferring the ice and water cloud optical properties over large areas could be developed, utilizing the information content in these bands based on different sensitivities of cloud reflection/absorption to cloud optical properties for each band.

We describe a novel approach developed for the NPOESS/VIIRS to retrieve pixel-level mixed-phase cloud optical thicknesses and effective particle sizes using 0.67, 1.6, 2.25, and 3.7 μm bands reflectance/radiance. Section 2 describes the retrieval methodology and mixed-phase cloud optical properties used in forward radiative transfer modeling subject to correction schemes. Section 3 presents retrieval results for two selected midlatitude Moderate Resolution Imaging Spectroradiometer (MODIS) proxy scenes containing widespread mixed-phase clouds, their comparison with the MODIS cloud products, and the assessment of retrieval performance using data from airborne *in situ* observations and space-based CloudSat data. Lastly a summary is given in Section 4.

2. Theoretical Description of the Retrieval Approach

A. Retrieval Algorithm

Four parameters are needed to describe a mixed-phase cloud: ice optical thickness τ_i, water optical thickness τ_w, ice crystal mean effective size D_e, and water droplet mean effective radius r_e. The retrieval algorithm follows the numerical iterative approach to search for the converged solution of (τ_i, τ_w) and (D_e, r_e) that is associated with minimal differences between simulated and observed reflectance/radiance for all four bands. Figure 1 shows the flowchart for retrieving (τ_i, τ_w) and (D_e, r_e). First of all, an adding–doubling radiative transfer model is used to build a library of cloud-only radiative parameters for all combinations of reference values of (τ_i, τ_w) and (D_e, r_e). For each pixel identified as mixed-phase cloud, reflectance/radiance at the four bands and viewing-geometry data are extracted from the MODIS L1B products. Required input parameters include cloud-top temperature T_c, cloud-top pressure P_c, surface albedos A_g, and surface temperature T_g. Parameters T_c and P_c are extracted from the MODIS Level 2 cloud products. A_g for the 0.645, 1.64, and 2.13 μm bands are compiled from the MODIS 16-day L3 1 km global albedo data product MOD43B3, and A_g for the 3.75 μm band and T_g is estimated from the MODIS 8-Day L3 global surface temperature/emissivity data product MOD11C2.

Depending on the sun-sensor geometry, a comprehensive set of cloud-only reflectances/radiances for combinations of reference (τ_i, τ_w) and (D_e, r_e) are first computed and tabulated. For a cloudy pixel, various pixel-dependent correction schemes to account for the Rayleigh scattering at the 0.645 μm band, the above-cloud water vapor absorption, and the 3.75 μm band thermal emission are then applied, and a lookup library of total reflectance/radiance is built for the retrieval of cloud parameters [17].

The mixed-phase cloud parameters are retrieved from a numerical search method using the aforementioned lookup library of reflectances/radiances for ice-water precomputed from an adding–doubling radiative transfer program. For each cloudy pixel subject to retrieval, the lookup library is fixed throughout the numerical iteration procedure. We first prescribe initial values of $r_e^{[0]}$ and $D_e^{[0]}$. We then calculate the 0.67 μm reflectance lookup table (LUT). Subsequently we retrieve $\tau^{[n]}$ using a 0.67 μm reflectance measurement through a numerical iterative search scheme, in which the difference between

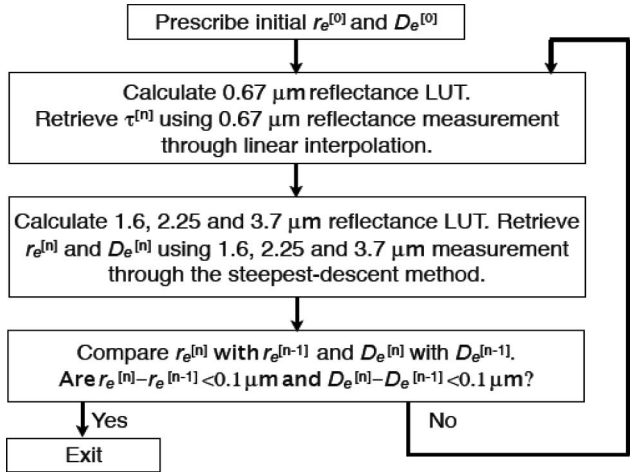

Fig. 1. Flowchart of the mixed-phase cloud retrieval approach.

measured and precomputed 0.67 μm reflectances are minimized. Next we calculate 1.6, 2.25, and 3.7 μm reflectance LUTs. We then retrieve $r_e^{[n]}$ and $D_e^{[n]}$ using 1.6, 2.25, and 3.7 μm measurements through the steepest-descent iterative search method. Finally we compare $r_e^{[n]}$ with $r_e^{[n-1]}$ and $D_e^{[n]}$ with $D_e^{[n-1]}$. If $r_e^{[n]} - r_e^{[n-1]} < 0.1\,\mu$m and $D_e^{[n]} - D_e^{[n-1]} < 0.1\,\mu$m, the iteration stops. Otherwise the iteration continues. The convergence threshold 0.1 μm was prescribed out of consideration for balance between retrieval accuracy and computational speed.

B. Optical Property Models

We have developed microphysics and optical property models for mixed-phase clouds. The microphysics models for ice clouds are based on *in situ* size distributions collected during field campaigns [18]. The microphysics models for water clouds are based on the functional form of modified Gamma size distributions [19]. Single-scattering properties for randomly oriented hexagonal ice crystals and spherical water droplets were obtained from a geometric optics ray-tracing method [20] and the Mie scattering theory, respectively. The bulk single-scattering properties for a mixed-phase cloud layer are parameterized following the formulations for combined cloud particles and gas developed by Fu and Liou [21]:

$$\widetilde{\omega} = \frac{\tau_s}{\tau} = \frac{\widetilde{\omega}_i\tau_i + \widetilde{\omega}_w\tau_w}{\tau_i + \tau_w} = \frac{\widetilde{\omega}_i\beta_i + \widetilde{\omega}_w\beta_w}{\beta_i + \beta_w}, \tag{1}$$

$$\widetilde{\omega}_l = \frac{\widetilde{\omega}_i\tau_i\widetilde{\omega}_{il} + \widetilde{\omega}_w\tau_w\widetilde{\omega}_{wl}}{\widetilde{\omega}_i\tau_i + \widetilde{\omega}_w\tau_w}, \tag{2}$$

$$f = \frac{\tau_{si}f_i + \tau_{sw}f_w}{\tau_s}, \tag{3}$$

where $\widetilde{\omega}$, $\widetilde{\omega}_l$, and f are mixed-phase single-scattering albedo, Legendre polynomial expansion coefficients, and phase function truncation factor, respectively. Parameters τ_s, τ, and β are the scattering optical thickness, total optical thickness, and extinction coefficient, respectively, with subscripts i and w denoting ice and water clouds. These optical properties models are determined from light-scattering computations weighted by the fractions of ice and water cloud particles in the mixed-phase clouds.

Figure 2 shows the single-scattering coalbedos ($=1-\widetilde{\omega}$) plotted as functions of D_e for 0.67 [Fig. 2(a)], 1.6 [Fig. 2(b)], 2.25 [Fig. 2(c)], and 3.7 μm [Fig. 2(d)] bands. The curves denote constant-r_e coalbedo values. It is noted that the coalbedos increases with increasing ice and water cloud particle sizes due to increased absorption. Moreover, these coalbedo values are sensitive to each combination of D_e and r_e forming the basis for the simultaneous retrieval of ice and water particle sizes. Figure 3 shows phase functions plotted as functions of scattering angle for 0.67 [Fig. 3(a)], 1.6 [Fig. 3(b)], 2.25 [Fig. 3(c)], and 3.7 μm [Fig. 3(d)] bands. In each frame, phase functions for pure ice cloud ($D_e = 42\,\mu$m), pure water cloud ($r_e = 8\,\mu$m), and a mixed-phase cloud ($D_e = 42\,\mu$m and $r_e = 8\,\mu$m) are plotted. It is noted that phase function values for the mixed-phase cloud at side-scattering angles are between those for pure ice and water, while at back-scattering angles, phase function values for the mixed-phase cloud are closer to those for pure water than for ice. Further investigations are needed to examine these behaviors.

C. Formulation and Modeling of Radiative Transfer

For any given cirrus cloudy pixel identified by the NPOESS/VIIRS cloud/phase mask programs, the retrieval algorithm uses a lookup library of reflectance/radiance at the four spectral bands to retrieve (τ_i, τ_w) and (D_e, r_e). For each spectral band, the dimension of the lookup library is $14(\tau_i) \times 16(\tau_w) \times 6(D_e) \times 9(r_e)$. For ice cloud the prescribed reference τ_i values are 0.125, 0.25, 0.5, 1, 2, 3, 4, 5, 6, 7, 8, 9, 10, and 12, and reference D_e values are 23.9, 30.4, 41.5, 71, 93, and 124 μm. For water cloud the reference τ_w values are 0.125, 0.25, 0.5, 1, 2, 3, 4, 5, 6, 8, 12, 16, 24, 32, 48, and 64, and the reference r_e values are 2, 3, 4, 6, 8, 12, 16, 24, and 32 [18]. We used an adding–doubling radiative transfer code specifically designed for simulating the radiative transfer in a mixed-phase cloud. The adding–doubling method has been recognized as a very powerful tool for multiple-scattering calculations, particularly with reference to remote sensing applications [22].

For each combination of (τ_i, τ_w) and (D_e, r_e), the adding–doubling radiative transfer model was used to calculate cloud-only radiative parameters, which include the bidirectional transmission functions (T and T^*), reflection functions (R and R^*), the transmission (γ and γ^*), the reflection (r and r^*), and the spherical albedo ($\bar{r}^*$). The latter three quantities are determined based on the following:

$$\gamma^{(*)}(\mu) = \frac{1}{\pi}\int_0^{2\pi}\int_0^1 T^{(*)}(\mu', \mu, \varphi - \varphi')\mu' \mathrm{d}\mu' \mathrm{d}\varphi' + e^{-\tau/\mu}, \tag{4}$$

$$r^{(*)}(\mu) = \frac{1}{\pi}\int_0^{2\pi}\int_0^1 R^{(*)}(\mu', \mu, \varphi - \varphi')\mu' \mathrm{d}\mu' \mathrm{d}\varphi', \tag{5}$$

$$\bar{r}^* = 2\int_0^1 r^*(\mu)\mathrm{d}\mu, \tag{6}$$

where μ and μ' are cosines of zenith angles for the outgoing and incoming directions, respectively. The superscript $*$ denotes the property related to incident radiation at cloud base. The μ values are discretized into eight Radau quadrature points within the interval (0,1), and the relative azimuthal angle between the sun and the sensor ($\Delta\varphi$) ranges between 0° to 180°, with an interval of 30°. For prescribed sun-sensor geometry, simulated cloud-only properties (T, T^*, R, R^*, r, r^*, γ, and γ^*) are calculated through linear interpolation between reference directions.

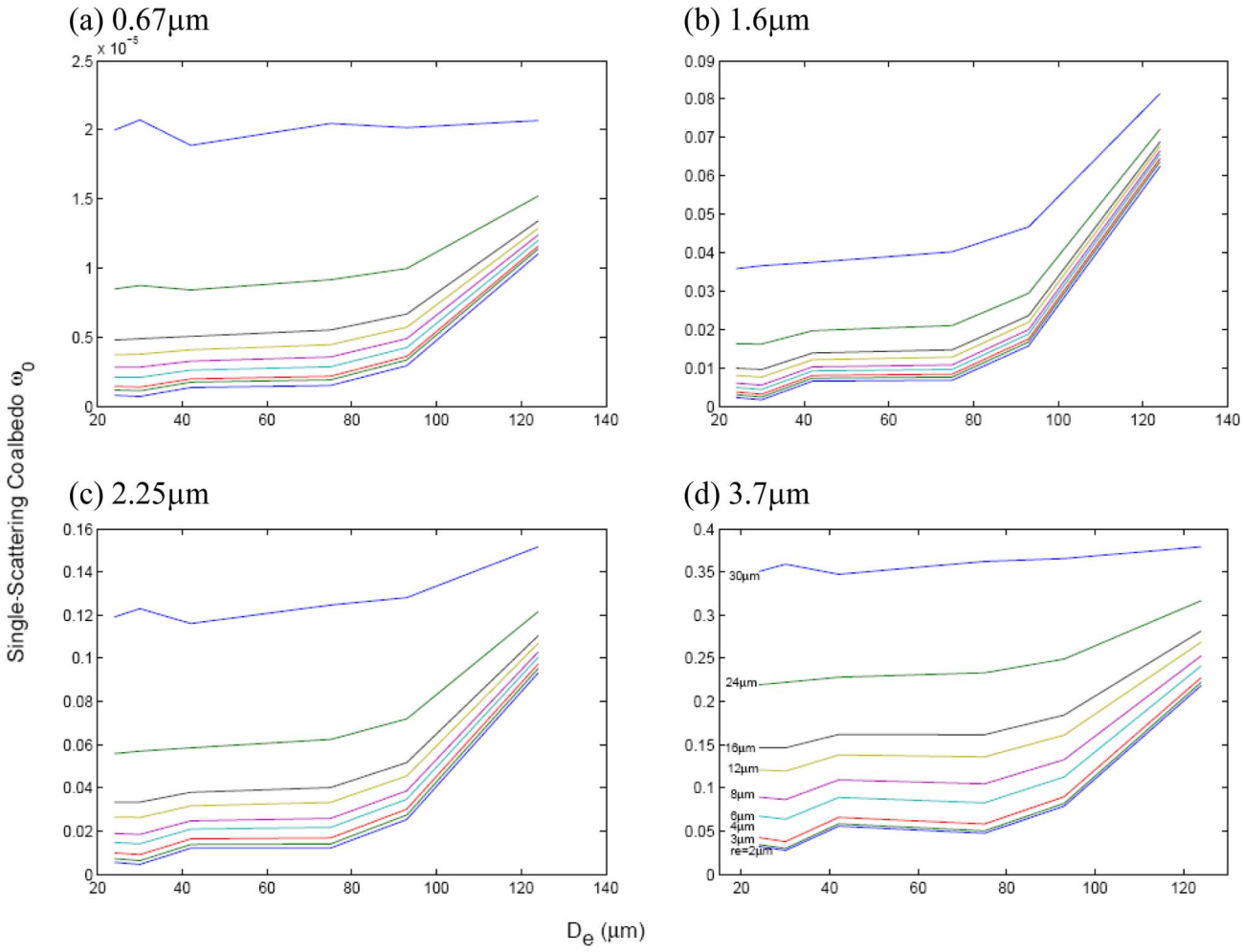

Fig. 2. (Color online) Single-scattering coalbedos plotted as functions of D_e for (a) 0.67, (b) 1.6, (c) 2.25, and (d) 3.7 μm bands. The curves denote coalbedo values of constant r_e.

Spherical albedo $\bar{r}^*$ is not affected by viewing geometry and does not require interpolation.

The observed total reflectance consists of cloud-only reflectance and the multiple reflection between surface and clouds [23]:

$$R(\mu,\mu_0,\Delta\varphi) = R_c(\mu,\mu_0,\Delta\varphi) + \frac{A_g}{1-\bar{r}^* A_g}\gamma^*(\mu)\gamma(\mu_0). \tag{7}$$

Water vapor absorption above the cloud is accounted for by assuming the atmosphere above cloud is purely absorptive [24]. The water vapor corrected reflectance R_w is approximated by the following:

$$R_w = RT_u(\mu)T_u(\mu_0), \tag{8}$$

where $T_u(\mu_0)$ and $T_u(\mu)$ are transmittances in the solar incident and satellite viewing directions, respectively. $T_u(\mu)$ is expressed as

$$T_u(\mu) = e^{-\tau_u(P_c)/\mu}, \tag{9}$$

where $\tau_u(P_c)$ is the water vapor absorption optical thickness for air mass above the cloud-top pressure P_c. The optical thickness $\tau_u(P_c)$ is calculated from the correlated-k-distribution method by assuming the water vapor profile in the U.S. Standard Atmosphere. A library of precomputed $\tau_u(P_c)$ is constructed. We assume there is no haze or aerosols above the clouds.

The Rayleigh scattering effect is more prominent in the 0.645 μm band than in the other three near-IR bands. Wang and King [25] showed that neglecting Rayleigh scattering correction can cause a significant error in retrieved τ_c for large solar and/or viewing zenith angles. To account for the Rayleigh scattering above clouds, we adopted their Rayleigh scattering parameterization scheme. The corrected bidirectional reflectance $R_{0.645}$ is expressed as

$$\begin{aligned} R_{0.645}(\mu,\mu_0,\Delta\varphi) \cong & \frac{\tau_r P^r(\mu,\mu_0,\Delta\varphi)}{4\mu\mu_0} \\ & + R_w(\mu,\mu_0,\Delta\varphi)e^{-\tau_r(1/\mu+1/\mu_0)} \\ & + \frac{\tau_r}{2\mu_0} r(\mu) e^{-\tau_r/\mu} \\ & + \frac{\tau_r}{2\mu} r(\mu_0) e^{-\tau_r/\mu_0}, \end{aligned} \tag{10}$$

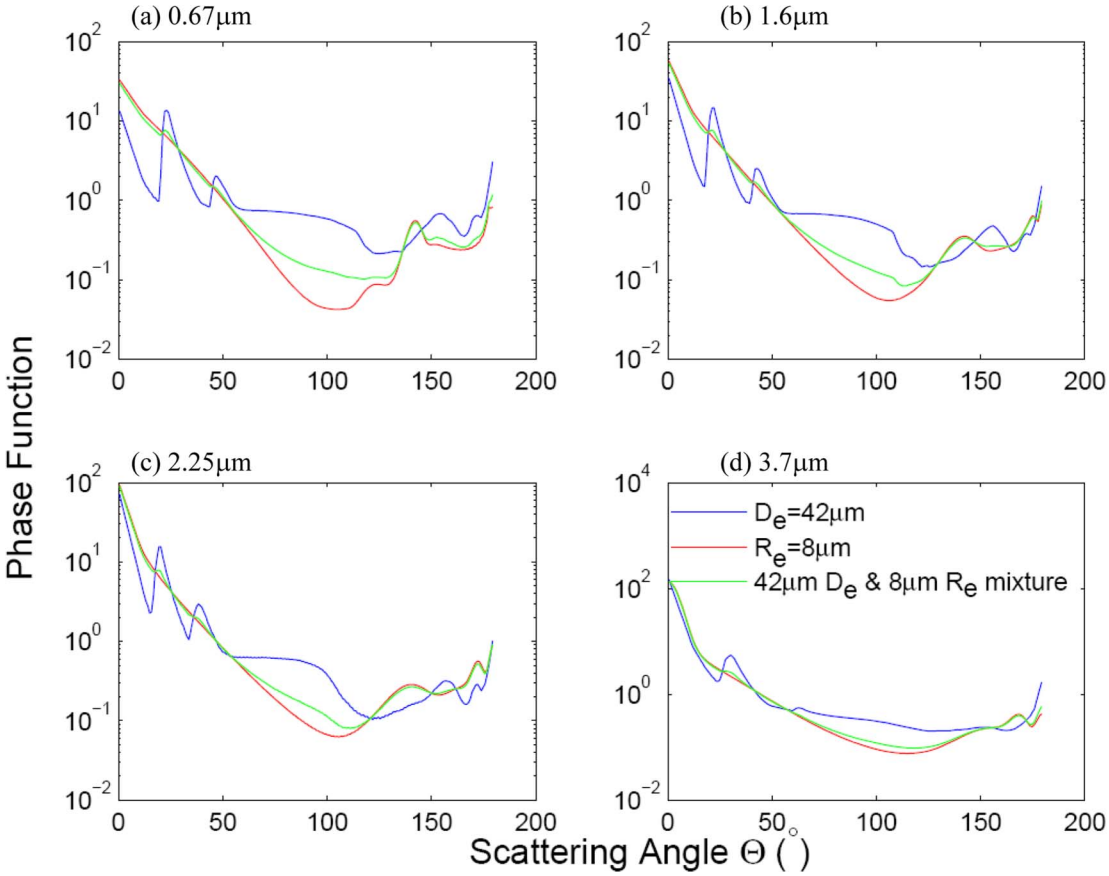

Fig. 3. (Color online) Phase functions plotted as functions of scattering angle for (a) 0.67, (b) 1.6, (c) 2.25, and (d) 3.7 μm bands. In each frame, phase functions for pure ice cloud ($D_e = 42\,\mu$m), pure water cloud ($r_e = 8\,\mu$m), and a mixed-phase cloud ($D_e = 42\,\mu$m and $r_e = 8\,\mu$m) are plotted.

where P^r is the Rayleigh scattering phase function, and τ_r is the Rayleigh optical thickness and can be calculated from P_c [22]. The first and second terms on the right-hand side account for the direct Rayleigh scattering without cloud reflection and for the reflection of direct solar radiation by the cloud, respectively. The third and fourth terms are for the reflection of the direct solar radiation by the cloud subject to single-scattering in the air and for single scattering in the air subject to the reflection from the cloud, respectively.

For the 3.75 μm band, the thermal emission from both Earth surface and cloud is a major component of the total measured radiance. The total radiance $I_{3.75}$ can be approximated by the following [23]:

$$I_{3.75}(\mu,\mu_0,\Delta\varphi) = R_w(\mu,\mu_0,\Delta\varphi)\frac{\mu_0 F_0}{\pi} + T_u(\mu)\left[\gamma^*(\mu)\frac{1-A_g}{1-\bar{r}^* A_g}B(T_g) + [1-\gamma(\mu)-r(\mu)]B(T_c)\right], \quad (11)$$

where B is the Planck function, F_0 is the extraterrestrial solar flux at the 3.75 μm band, and T_c and T_g are cloud and surface temperatures, respectively. The first term on the right-hand side represents the reflected solar radiance, corrected for multiple reflections and water vapor absorption. The second term denotes the contribution from surface and cloud emissions attenuated by above-cloud water vapor absorption $T(\mu)$. For each mixed-phase cloudy pixel, these corrections are applied to all combinations of reference (τ_i, τ_w) and (D_e, r_e) to create a lookup library of reflectance/radiance.

3. Application to MODIS Proxy Scenes

The capability of this new approach was demonstrated using the MODIS 0.645,1.64, 2.13, and 3.75 μm bands reflectance/radiance data as a proxy to VIIRS. Here we present results of the application of the retrieval algorithm to two MODIS mixed-phase cloudy cases. The first scene over North Platte, Nebraska, was observed by MODIS/Terra on 14 October 2001, and the quality of its retrieval results were evaluated by comparison with the MODIS cloud products and cloud properties derived from airborne *in situ* observations. The second scene over the Great Lake region and Eastern Canada was observed by the A-Train's MODIS/Aqua, and retrieval results were compared with Cloud Profiling Radar (CPR)/CloudSat cloud data products.

A. North Platte, Nebraska, 14 October 2001 at 1720 UTC

A proxy scene, 14 October 2001 over North Platte, Nebraska, during the ninth Cloud Layer Experiment (CLEX-9), was analyzed. The field campaign CLEX has provided a series of aircraft measurements to improve the understanding of mixed-phase nonprecipitating clouds in the middle troposphere. The last of these experiments, the CLEX-9, took place over North Platte, Nebraska, from October to November 2001.

For the case of 14 October, a 300 m thick supercooled liquid droplet layer was present at the top of the cloud, and a roughly 2000 m thick ice particle layer was distributed in the lower part of cloud [16]. A narrow zone between the two layers was actually mixed-phase (i.e., contained both ice and liquid water particles). The temperature varied from −10 °C at the cloud base to −22 °C at cloud top. The temperature at the peak of the liquid droplet layer was −22 °C, and the peak of ice layer was −13 °C. The University of Wyoming King Air (UWKA) research aircraft sampled the southern edge of the cloud feature at approximately 5300 m near cloud top. The aircraft observations closely coincided with the Terra satellite overpass. The aircraft was equipped with a variety of observational instruments and probes. The UWKA aircraft penetrated each layer and measured ice particle and water droplet size distributions and cloud particle habit fractions in each specific layer. The ice particle size distributions were obtained by Particle Measurement Systems (PMS) OAP2D-C with 20 bins. Water droplet size distributions were measured by PMS FSSP-100 with 16 bins. Ice particle habits in the mixed-phase cloud were measured from the two-dimensional imagery of particles by the PMS-2DC cloud probe. The liquid particle fraction was obtained from the FSSP-100 observations. Other simultaneous observations of liquid water content and droplet size distribution were made by a Droplet Measurement Technology model LWC-100, a Rosemount 871FA icing detector, and a Gerber PVM-100A.

Figure 4 shows images of mixed-phase retrieved τ_i [Fig. 4(a)], D_e [Fig. 4(b)], τ_w [Fig. 4(c)], and r_e [Fig. 4(d)]. It is noted that, in general, $\tau_i < \tau_w$, and this is physically reasonable since the observed mixed-phase cloud might have been in its initial glaciation stage, whereby ice crystals were beginning to form through the Bergeron–Findeison process. It is also noted that, in general, $D_e > 2r_e$, and this is consistent with typical measurements of water and ice cloud particle distributions. Also shown are retrieved τ_i and τ_w versus MODIS τ_c within the pink box [Fig. 4(e)] and retrieved D_e and r_e versus MODIS r_e within the pink box [Fig. 4(f)]. These comparisons show that the sum of τ_i and τ_w are roughly equal to MODIS τ_c. On the other hand, the mixed-phase r_e is smaller than MODIS r_e, while many mixed-phase D_e are larger than 2 times the MODIS r_e. Figure 5 shows the comparison of MODIS-retrieved *in situ* r_e for collocated pixels. Because of the limitation in the collocation process, there is only a total of 11 comparisons, 3 for water cloud and 8 for ice cloud. Both retrieved and observed ice clouds r_e ($=D_e/2$) range between 15 and 50 μm, showing good agreement. The retrieved water cloud r_e is of the order of 10 μm, which is smaller than observed values (15–20 μm). The mean differences are around 2 μm, which meets the accuracy requirement of VIIRS, indicating preliminary success from the retrieval approach.

B. Great Lakes and Eastern Canada, 9 November 2006 at 1800 UTC

This case was observed during the Canadian CloudSat/Cloud-Aerosol Lidar and Infrared Pathfinder Satellite Observations (CALIPSO) Validation Project (C3VP) field campaign. The MODIS/Aqua flew over the Great Lakes region and Eastern Canada on 9 November 2006 at 1800 UTC followed by CloudSat and CALIPSO. The MODIS true color composite image [Fig. 6(a)] displays a large area of mixed-phase and cirrus clouds over Eastern Canada, as indicated by cloud mask/phase results. The blue arrow denotes the CloudSat track. For the purpose of assessment of retrieval performance using CPR/CloudSat observations, a rectangular area centered along the CloudSat track was selected, as indicated by the red box.

Figures 6(b)–6(d) show retrieved τ_c ($=\tau_i + \tau_w$), D_e, and r_e for mixed-phase cloudy pixels within the selected box, respectively. For the whole box, the total optical thickness τ_c ranges between 0 and 100, and optically thick clouds were mostly scattered over the western half of the selected box. Most pixels are associated with large D_e (mostly around 120 μm), and pixels with smaller D_e (<60 μm) were scattered among them. Retrieved r_e for many pixels are smaller than 10 μm, but within the southeast quadrant, r_e are larger than 10 μm. Also shown are retrieved τ_i and τ_w versus MODIS τ_c within the pink box [Fig. 6(e)] and retrieved D_e and r_e versus MODIS r_e within the pink box [Fig. 6(f)]. These comparisons show that τ_i are all smaller than MODIS τ_c, but roughly half of τ_w are larger than MODIS τ_c, and half of τ_w are larger than MODIS τ_c. This distribution pattern is different from that shown in Fig. 4(e). It must be noted that many pixels are optically thick with $\tau_c > 20$ compared to the optically thin cloudy case of Fig. 4. For optically thick clouds, retrieval uncertainty increases with optical depth [18], and therefore differences between τ_c from mixed-phase and the MODIS retrievals also increase. On the other hand, the mixed-phase r_e is smaller than MODIS r_e, while many mixed-phase D_e are larger than 2 times the MODIS r_e. This pattern is consistent with that shown in Fig. 4(f).

To compare retrieval results with collocated CloudSat data products within the selected box, we further identified a section of the CloudSat track in which the mixed-phase cloud coverage is continuous. This section corresponds to a 14 s CloudSat overpass from 18:04:24 to 18:04:38 UTC. Within this period, mixed-phase clouds occurred between 4 and 9 km. To assess

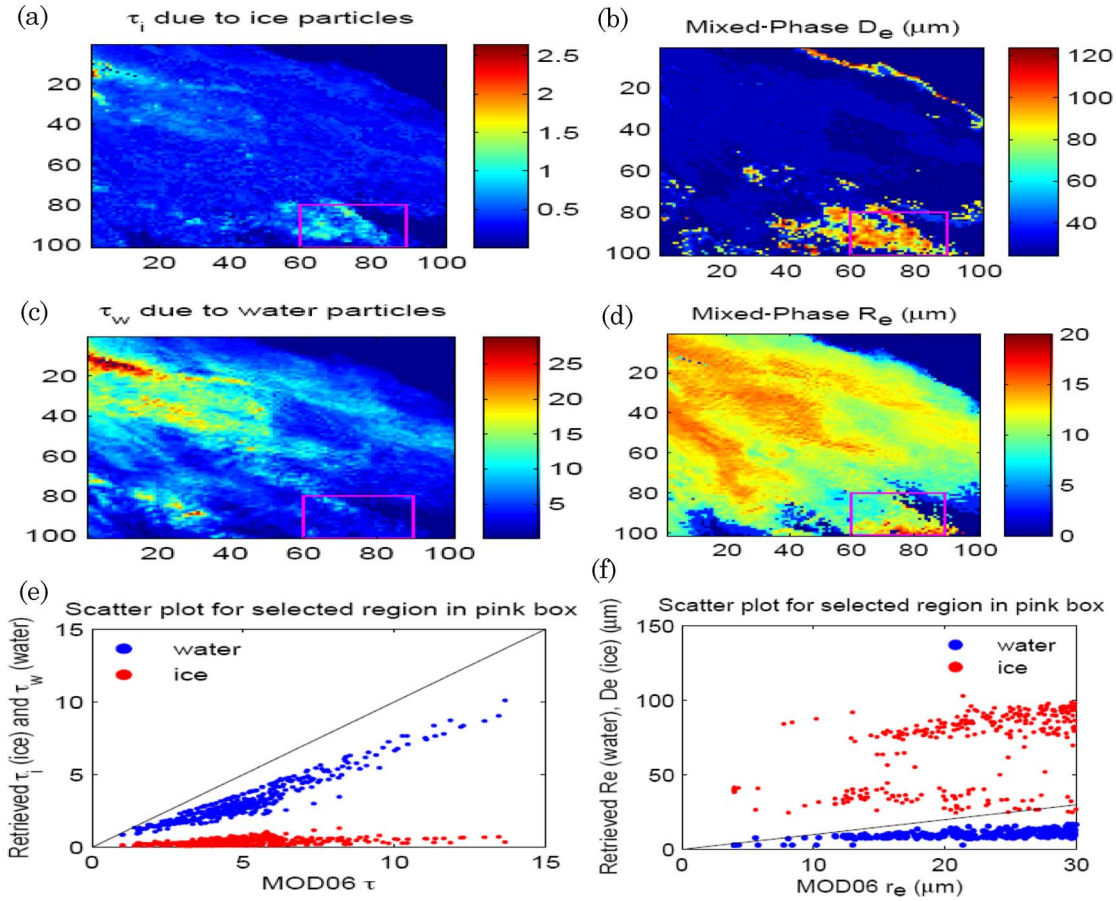

Fig. 4. (Color online) Images of mixed-phase retrieved (a) τ_i, (b) D_e, (c) τ_w, and (d) r_e for the Terra/MODIS scene of 14 October 2001 over North Platte, Nebraska. Also shown are (e) retrieved τ_i and τ_w versus MODIS τ within the pink box and (f) retrieved D_e and r_e versus MODIS r_e within the pink box.

the validity of retrieved cloud ice water paths (IWPs) and mean sizes, we processed CloudSat D_e and ice water content (IWC) profiles, where the MODIS IWP was obtained from the following [21]:

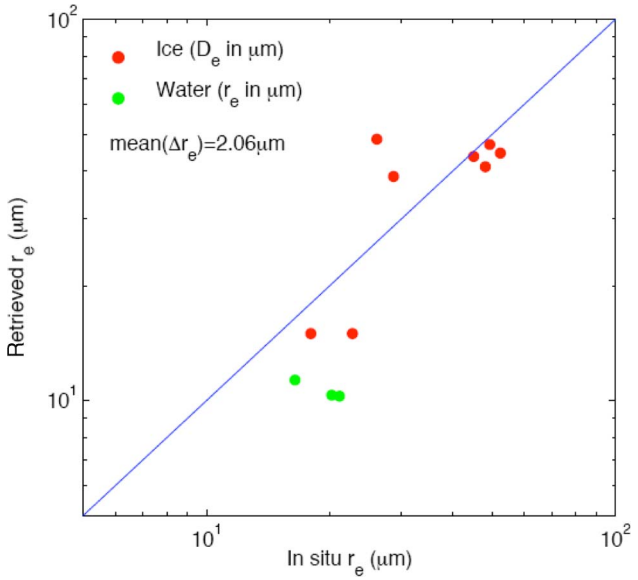

Fig. 5. (Color online) Comparison of retrieved and *in situ* r_e for collocated pixels.

$$\mathrm{IWP} \approx \tau_c/(a + b/D_e), \tag{12}$$

and CloudSat IWP was obtained by the vertical integration of IWC from cloud base to cloud top and collocation of the MODIS and CloudSat cloud parameters. Figures 7(a) and 7(b) show the time series of CloudSat-derived vertical profiles of D_e and IWC, respectively. It is noted that there are occurrences of $D_e > 200\,\mu$m for the first and last 4 s. For the middle section, $D_e < 150\,\mu$m. Also, for the first 4 s, IWC $> 0.1\,\mathrm{gm\,m^{-3}}$, while for the rest of the period, IWC $< 0.1\,\mathrm{gm\,m^{-3}}$. Figures 7(c) and 7(d) show the time series of the MODIS- and CloudSat-derived vertical profiles of D_e and IWC, respectively. MODIS-retrieved D_e are generally smaller than collocated CloudSat D_e due to the fact that the CPR is mainly sensitive to large particles and missing smaller particles. Comstock *et al.* [26] show a case that ground-based Millimeter Cloud-Wave Radar completely missed a thin cirrus cloud layer detected by collocated Micro-Pulse Lidar deployed at the Atmospheric Radiation Measurements Western Pacific Region site. Moreover, differences in MODIS and CloudSat D_e are smaller for the middle period than for the first and last 4 s. This is because the sensitivity of near-IR bands reflectance to D_e is weaker for larger D_e. On the other hand, MODIS-retrieved IWP match

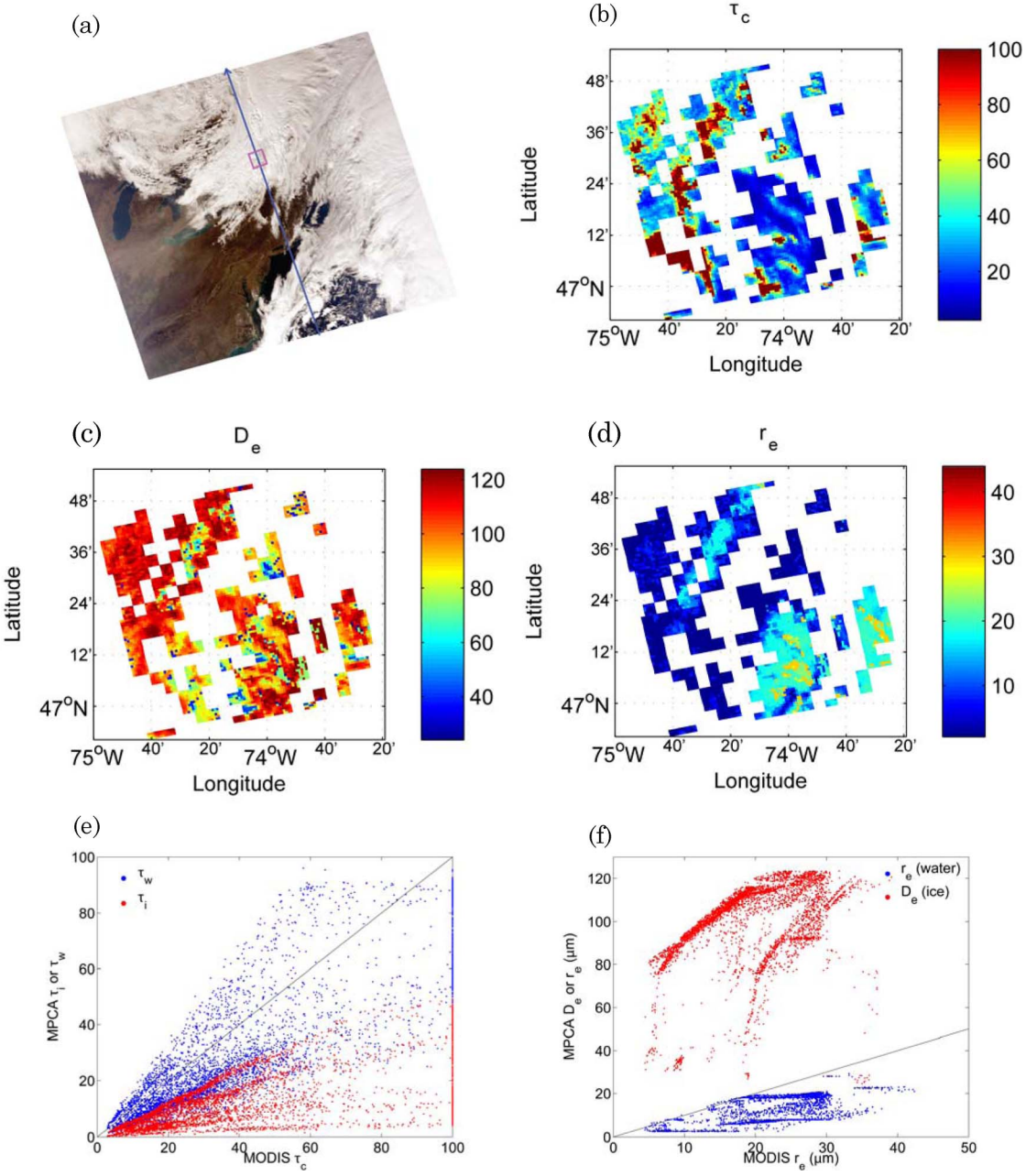

Fig. 6. (Color online) Images of mixed-phase retrieved for the Terra/MODIS scene of 9 November 2006 over the Great Lakes region and Eastern Canada: (a) MODIS composite image, where the blue arrow denotes the CloudSat/CALIPSO track and the red box denotes the selected domain for validation of the retrieval algorithm; (b) τ_c; (c) D_e; and (d) r_e within the red box. Also shown are (e) retrieved τ_i and τ_w versus MODIS τ_c and (f) retrieved D_e and r_e versus MODIS r_e within the red box.

CloudSat IWP up to $t = 8$ s. For $t > 8$ s the MODIS IWP is larger than the CloudSat IWP. A possible explanation is that, for $t < 8$ s, large particles dominate the size distribution, so the two IWPs are approximately the same, while for $t > 8$ s, small particles dominate the size distribution, and CloudSat substantially underestimates IWP.

4. Summary

Many middle-level clouds are mixed phase and their global cloud coverage is significant. The presence of these mixed-phase clouds could be an important factor in the global radiation budget and climate system. Reliable algorithms for the detection of mixed-phase cloudy conditions and the retrieval of their optical properties by ground-based and spaceborne sensors are urgently needed for improved parameterizations of cloud microphysics, dynamics, and radiative transfer processes in numerical weather prediction and climate models. In the current NPOESS/VIIRS cloud retrieval program, separate cloud optical property algorithms are applied to mixed-phase cloudy pixels, which are treated either as water cloud or as ice cloud. With the availability of

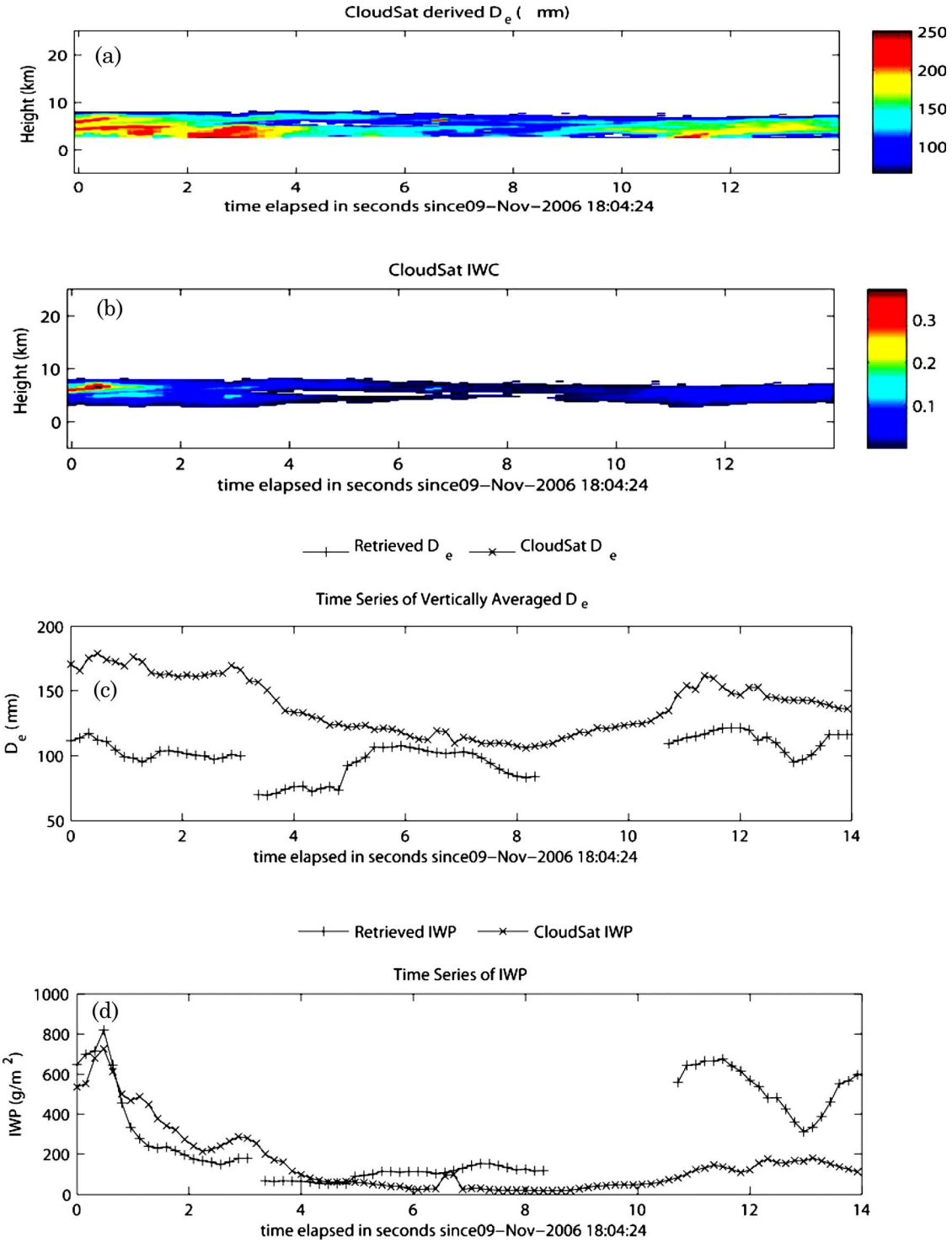

Fig. 7. (Color online) (a) Time series of vertically resolved D_e derived from CPR observations. (b) Same as in (a) except for IWC. (c) Collocated time series of retrieved and CPR $D_e(t)$. (d) Same as in (c) except for IWP.

multiple visible and near-IR band radiance data from VIIRS, it appears that a retrieval scheme for inferring the ice and water cloud optical properties over large areas could be developed, utilizing the information content in these bands based on different sensitivities of cloud reflection/absorption to cloud optical properties for each band.

A novel lookup table approach for the NPOESS/VIIRS to simultaneously retrieve ice and water optical thickness and effective particle sizes in a mixed-phase cloud layer was developed. This approach uses a numerical iterative search method based on a lookup library of precomputed reflectances/radiances from an adding–doubling radiative transfer

program, subject to corrections for Rayleigh scattering at the 0.645 μm band, above-cloud water vapor absorption, and 3.75 μm band thermal emission.

The capability of this new approach was demonstrated using MODIS data as proxy to VIIRS. Two proxy scenes, 14 October 2001 over North Platte, Nebraska, during CLEX-9 with the support of collocated airborne *in situ* measurements and 9 November 2006 over the Great Lakes and Eastern Canada during C3VP with the support of collocated CloudSat data. The retrieved cloud optical thicknesses and mean effective sizes were first examined by comparison with the MODIS cloud products. These assessments show that retrieved cloud optical thicknesses and mean effective sizes correlate well with the MODIS cloud products for both cases. It is shown that the sum of τ_i and τ_w are roughly equal to the MODIS τ_c for small values of τ_c. On the other hand, the mixed-phase r_e is smaller than MODIS r_e, while many mixed-phase D_e are larger than 2 times the MODIS r_e, as expected. The quality of retrieved cloud particle sizes for the CLEX-9 case was evaluated by comparison with collocated *in situ* measurements during UWKA flights. Retrieved ice crystal mean effective sizes are generally well correlated with mean sizes derived from 2D-C measurements, but retrieved water droplet mean effective sizes are generally smaller in magnitude. The retrieved cloud particle sizes and cloud water path for the C3VP case was evaluated by comparison with collocated CloudSat data products. Retrieved ice crystal mean effective sizes are generally smaller than CloudSat mean sizes, because CloudSat radar tends to miss smaller particles. Overall the mixed-phase retrieval algorithm represents a step of progress in the development of satellite cloud retrieval program in terms of its capability to determine the mixed-phase cloud properties and is potentially applicable to processing remote sensing data from the next generation VIIRS/ NPOESS and ABI/GOES-R, which are to be launched beyond 2010 and 2014, respectively.

This research was supported by Northrop Grumman Space Technology (NGST) contract 97904DDM3S managed by A. Dybdahl and M. Mussetto, by National Science Foundation (NSF) grant 0331550, and by U.S. Department of Energy (DOE) grant DEFG03-00ER62904.

References

1. Z. Sun and K. P. Shine, "Parameterization of ice cloud radiative properties and its application to the potential climatic importance of mixed-phase clouds," J. Clim. **8**, 1874–1888 (1995).
2. K. N. Liou, Q. Yue, Y. Gu, and G. MacFarquhar, "On the correlation between ice water content and ice crystal size and its application to radiative transfer and general circulation models," Geophys. Res. Lett. **35**, L13805 (2008).
3. B. Henson, "Smoother skies," UCAR Quarterly Winter 2007–2008, 8–11 (2008).
4. C. M. R. Platt, "Lidar observation of a mixed-phase altostratus cloud," J. Appl. Meteorol. **16**, 339–345 (1977).
5. K. Sassen and K. N. Liou, "Scattering of polarized laser light by water droplet, mixed-phase and ice crystal clouds. Part I: angular scattering patterns," J. Atmos. Sci. **36**, 838–851 (1979).
6. H. Jiang, W. R. Cotton, J. O. Pinto, J. A. Curry, and M. J. Weissbluth, "Cloud resolving simulations of mixed-phase Arctic stratus observed during BASE: sensitivity to concentration of ice crystals and large-scale heat and moisture advection," J. Atmos. Sci. **57**, 2105–2117 (2000).
7. G. McFarquhar and S. G. Cober, "Single-scattering properties of mixed-phase Arctic clouds at solar wavelengths: impacts on radiative transfer," J. Clim. **17**, 3799–3813 (2004).
8. Q. Fu and S. Hollars, "Testing mixed-phase cloud water vapor parameterizations with SHEBA/FIRE-ACE observations," J. Atmos. Sci. **61**, 2083–2091 (2004).
9. A. Tremblay, P. A. Vaillancourt, S. G. Cober, A. Glazer, and G. A. Isaac, "Improvements of a mixed-phase cloud scheme using aircraft observations," Mon. Weather Rev. **131**, 672–686 (2003).
10. M. D. Shupe, P. Kollias, S. Y. Matrosov, and T. L. Schneider, "Deriving mixed-phase cloud properties from Doppler radar spectra," J. Atmos. Ocean. Technol. **21**, 660–670 (2004).
11. P. Zuidema, B. Baker, Y. Han, J. Intrieri, J. Key, P. Lawson, S. Matrosov, M. Shupe, R. Stone, and T. Uttal, "An Arctic springtime mixed-phase cloudy boundary layer observed during SHEBA," J. Atmos. Sci. **62**, 160–176 (2005).
12. C. Flynn, A. Mendoza, D. D. Turner, J. Comstock, S. A. McFarlane, and J. Mather, "Observation of clouds and aerosol with elastic depolarization lidar during the Mixed-Phase Arctic Cloud Experiment (M-PACE)," presented at the 2nd AMS Symposium on Lidar Atmospheric Applications, San Diego, CA, 8–14 January 2005.
13. Z. Wang, K. Sassen, B. B. Demoz, and D. N. Whiteman, "Arctic mixed-phase cloud microphysical properties retrieved from Ground-based active and passive remote sensors," presented at the 8th AMS Conference on Polar Meteorology and Oceanography, San Diego, CA, 8–14 January 2005.
14. E. Wong, K. Hutchison, S. C. Ou, and K. N. Liou, "Cirrus cloud top temperatures retrieved from radiances in the National Polar-Orbiting Operational Environmental Satellite Syste—Visible Infrared Imager Radiometer Suite 8.55 and 12.0 μm band passes," Appl. Opt. **46**, 1316–1325 (2007).
15. A. Korolev, G. Isaac, S. Coberi, J. W. Strapp, and J. Hallett, "Microphysical characterization of mixed-phase clouds," Q. J. R. Meteorol. Soc. **129**, 39–65 (2003).
16. J. Niu, L. D. Carey, P. Yang, A. Kankiewicz, and T. H. Vonder Haar, "A common microphysical structure for midlevel mixed-phase cloud in the mid-latitudes: results from the Cloud Layer Experiment (CLEX-9)," presented at the 12th AMS Conference on Cloud Physics, Madison, WI, 9–14 July 2006, pp. 4.
17. X. Wang, K. N. Liou, S. S. C. Ou, G. G. Mace, and M. Deng, "Remote sensing of cirrus cloud vertical size profile using MODIS data," J. Geophys. Res. (to be published).
18. S.-C. Ou, Y. Takano, K. Liou, G. J. Higgins, A. George, and R. Slonaker, "Remote sensing of cirrus cloud optical thickness and effective particle size for the national polar-orbiting operational environmental satellite system visible infrared imager radiometer suite: sensitivity to instrument noise and uncertainties in environmental parameters," Appl. Opt. **42**, 7202–7214 (2003).
19. J. E. Hansen and L. D. Travis, "Light scattering in planetary atmospheres," Space Sci. Rev. **16**, 527–610 (1974).
20. Y. Takano and K. N. Liou, "Solar radiative transfer in cirrus clouds, Part I," J. Atmos. Sci. **46**, 3–19 (1989).
21. Q. Fu and K. N. Liou, "Parameterization of the radiative properties of cirrus clouds," J. Atmos. Sci. **50**, 2008–2025 (1993).
22. K. N. Liou, *An Introduction to Atmospheric Radiation*, 2nd ed. (Academic, 2002), pp. 583.

23. T. Y. Nakajima and T. Nakajima, "Wide-area determination of cloud microphysical properties from NOAA AVHRR measurements for fire and Astex regions," J. Atmos. Sci. **52**, 4043–4059 (1995).
24. S. Platnick, M. King, S. Ackerman, W. Menzel, B. Baum, J. Riedi, and R. Frey, "The MODIS cloud products—algorithms and examples from Terra," IEEE Trans. Geosci. Remote Sens. **41**, 459–473 (2003).
25. M. Wang and M. D. King, "Correction of Rayleigh scattering effects in cloud optical thickness retrievals," J. Geophys. Res. **102**, 915–926 (1997).
26. J. M. Comstock, T. P. Ackerman, and G. G. Mace, "Ground-based lidar and radar remote sensing of tropical cirrus clouds at Nauru Island: cloud statistics and radiative impacts," J. Geophys. Res. **107**, 4714 (2002).